

Effect of Heat Treatment on the Micro-/Defect-Structure and Tensile Behavior of Additively Manufactured A1000-RAM10 Aluminum Alloy

Md Faysal Khan^{1,2}, Reza Ghiaasiaan^{1,2}, Paul R. Gradl³, Shuai Shao^{1,2}, Nima Shamsaei^{1,2*}

¹National Center for Additive Manufacturing Excellence (NCAME), Auburn University,
Auburn, AL 36849, USA

²Department of Mechanical Engineering, Auburn University, Auburn, AL 36849, USA

³Propulsion Department, NASA Marshall Space Flight Center, Huntsville, AL 35812, USA

* Corresponding author:

Email: shamsaei@auburn.edu

Tel: (334) 844 4839

Abstract

This study investigated the effect of heat treatment (HT) on micro-/defect-structure and room temperature tensile behavior of A1000-RAM10 aluminum alloy fabricated using laser powder bed fusion. The alloy was produced via a reactive additive manufacturing strategy, incorporating 10 vol.% of Ti and B₄C inoculant particles into pre-alloyed A1000 powder. These particles acted as grain boundary pinners, promoting the formation of equiaxed grains. The post-processing HTs included stress relieving (SR) and hot isostatic pressing (HIP). HIP significantly reduced defect content compared to non-heat-treated and SR conditions. However, due to the presence of thermally stable particles (i.e., TiC and B₄C), the grain structure remained largely unchanged across all conditions. As a result, the yield and ultimate tensile strengths, and elongation to failure were comparable among the different HT conditions. These particles contributed to void nucleation, influencing both the failure mechanism and ductility of the alloy.

Keywords: Laser powder bed fusion (L-PBF/LB-PBF), A1000-RAM10, Heat treatment, Micro-/defect-structure, Tensile

Introduction

The A1000 series consists of wrought Al alloys that contain at least 99 wt.% Al, with impurity limits typically below 0.5 wt.% Fe and 0.2 wt.% Si [1]. This near-pure chemistry gives them excellent electrical and thermal conductivity, high reflectivity, and outstanding corrosion resistance. Consequently, A1000 alloys are widely employed in food-and-beverage packaging, lighting reflectors, electrical conductors, and building facades, where mechanical strength is not a primary concern. These components are commonly manufactured through conventional forming-based methods, including rolling, extrusion, and drawing, which are often followed by secondary machining operations. While these manufacturing routes are mature and well-understood, they have inherent drawbacks. For instance, rolling is primarily limited to producing flat sheets, and extrusion to simple cross-sectional profiles. These methods struggle to efficiently produce components with internal channels or intricate surface geometries. Additionally, the extensive material removal in subtractive processes leads to significant waste and increased production time, contributing to longer lead times and higher costs.

In addition to manufacturing limitations, the composition of A1000 alloys limits their mechanical performance. Their near-pure chemistry lacks alloying elements, which are typically required to form strengthening precipitates during age-hardening heat treatments. As a result, these alloys are categorized as non-heat-treatable and derive strength mainly through work-hardening mechanisms [2,3]. While these mechanisms offer moderate strength improvements, they are insufficient for structural applications where both reasonable strength and ductility are important.

Additive manufacturing (AM) presents an attractive alternative to expand the applications of AM A1000 alloys. AM methods enable the production of components with complex geometries and internal features, while reducing waste and simplifying the supply chain [4,5]. However, the AM of Al alloys remains challenging due to issues, such as poor flowability in the molten state and high solidification shrinkage, which can result in hot tearing and defect formation during solidification. To mitigate these challenges, a reactive additive manufacturing (RAM) approach, developed and patented by Elementum 3D [6], has been introduced. In this method, 10 vol.% of inoculant particles, such as Ti and B₄C, are incorporated into the feedstock of pre-alloyed A1000 powder. During solidification, the thermally stable B₄C and TiC (formed during the RAM process) particles act as heterogeneous nucleation sites and serve as grain boundary pinners to resist grain growth and produce a fine-grained and equiaxed microstructure [7].

Although A1000 alloys are traditionally non-heat-treatable, the addition of inoculant particles can lead to the formation of secondary phases during solidification, whose morphology and distribution may be influenced by the post-process heat treatments (HT). Therefore, this study investigates the effect of different HT conditions, including stress relieving (SR), hot isostatic pressing (HIP), and their combination on the microstructure, defect content, and room temperature tensile behavior of A1000-RAM10 alloy produced via laser powder bed fusion (L-PBF).

Experimental Procedure

The specimens in this study were fabricated using A1000-RAM10 powder, which was supplied by Elementum 3D. This powder was prepared through vacuum induction gas atomization of pre-alloyed A1000, followed by mechanical blending with RAM additives, such as Ti and B₄C. The chemical composition of the powder is listed in **Table 1**. The measurement was by inductively coupled plasma optical emission spectrometry (ICP-OES), except for O, N, and C contents. The O and N contents were determined using the inert gas fusion according to ASTM E1409-13 [8], and the C content was measured using the combustion infrared absorption method following ASTM E1019-18 [9]. Cylindrical rods with 14 mm diameter and 100 mm length were fabricated vertically via L-PBF using an EOS M290 machine using the following process parameters: laser power of 370 W, scanning speed of 1200 mm/s, hatch spacing of 0.19 mm, and layer thickness of 30 μ m. Ar was used as the shielding gas during fabrication.

Table 1. The chemical composition (wt.%) of A1000-RAM10 powder used in the study, obtained via ICP-OES by Elementum 3D.

Elements	Al	Ti	B	C	Fe	Si	Others
wt.%	Bal.	10.80	1.90	0.53	0.15	0.07	<0.50

After fabrication, two batches of cylindrical rods were subjected to HTs: one with stress relieving followed by hot isostatic pressing (SR+HIP), and the other with HIP only [10]. SR was performed at 300 °C for 2 hrs followed by furnace cooling and HIP was carried out at 510 °C under 100 MPa isostatic pressure for 2 hrs followed by furnace cooling.

Microstructural characterization was completed on coupons excised from cylindrical rods on the longitudinal plane (i.e., parallel to the build direction). One coupon was analyzed before the HT, labeled as non-heat treated (NHT) and the others were after two different HT conditions, labeled as HIP and SR+HIP. The coupons were mounted using epoxy resin and then ground and polished according to ASTM E3 [11]. Microscopy was conducted using a Zeiss Crossbeam 550 scanning electron microscope (SEM) equipped with electron backscatter diffraction (EBSD) and energy dispersive X-ray spectroscopy (EDS) detectors. Backscattered secondary electron (BSE) images were obtained using the electron channeling contrast imaging technique.

X-ray computed tomography (X-CT) was performed on a coupon of 5 mm diameter and 5 mm height, machined from the mid-section of the cylindrical rods, to evaluate the volumetric defect contents in different HT conditions. Scans were performed using a Zeiss Xradia 620 Versa system with a 60 kV accelerating voltage, 6.5 W power, and 5.3 μ m voxel size. Volumetric reconstruction was carried out using Zeiss proprietary software, followed by image analysis using ImageJ and Dragonfly software.

Following HTs, the cylindrical rods were machined to the final geometry of the tensile test specimens according to ASTM E8 [12] (see **Figure 1**). The uniaxial tensile tests were performed at room temperature (21 °C) using a constant strain rate of 0.005 mm/mm/min following ASTM E8 to accurately capture yield behavior. At least three specimens were tested at room temperature

for each condition (i.e., NHT and the two HTs) and the reported values for yield strength (YS), ultimate tensile strength (UTS), and elongation to failure (EL) represent the averages of these tests.

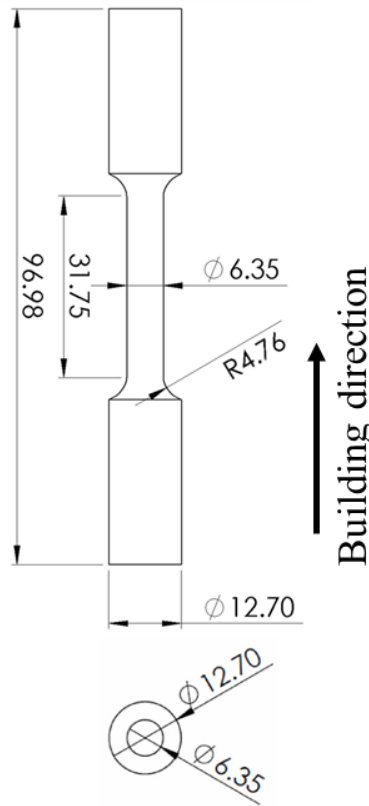


Figure 1. Tensile specimen geometry used in this study according to ASTM E8 [12]. All dimensions are in ‘mm’.

Results and Discussion

The defects within the three X-CT scanned volumes, including the NHT and two different HT conditions (i.e., HIP and SR+HIP), are presented in Figure 2(a)-(c). The histograms for the defect size distribution are also presented in Figure 2(d). The volumetric defect populations in the HIP and SR+HIP conditions (both at a relative porosity of 0.01%) were significantly lower than that in the NHT condition (relative porosity of 0.4%). The largest defect sizes, measured by the equivalent sphere diameter, were 92 μm , 42 μm , and 37 μm for the NHT, HIP, and SR+HIP conditions, respectively. These results indicate that HIP greatly reduced both the defect population and overall defect size compared to the NHT condition.

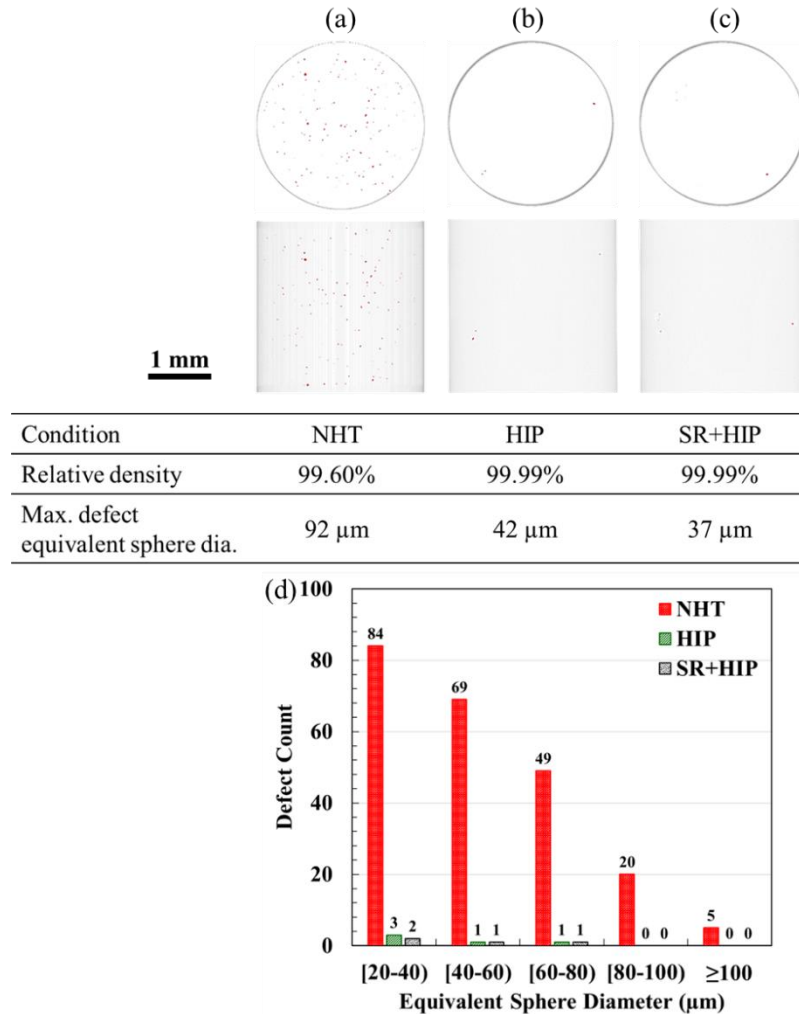


Figure 2. X-CT scan results for the L-PBF A1000-RAM10 coupons in NHT, HIP, and SR+HIP conditions presented using (a)-(c) 3D visualization of volumetric defects and (d) the corresponding defect size distributions.

The BSE micrographs along with the grain structures of the L-PBF A1000-RAM10 coupons on the longitudinal plane (i.e., the plane parallel to the build direction) in NHT, HIP, and SR+HIP conditions are presented in **Figure 3**. The particles, such as TiC and B₄C, were observed randomly distributed throughout the microstructure at lower magnifications (see **Figure 3(a)**). These particles remained stable for both HT conditions (see **Figure 3(c)** and (e)). In the micrographs, B₄C and TiC particles appeared in dark and bright contrast, respectively. At higher magnifications, some needle-shaped Al-Fe intermetallic phases, likely Al₃Fe, and a reaction layer composed of Al₃Ti and Ti₅Si₃ surrounding the TiC particles were also observed. These phases have been reported in various Al-Fe and Al-Si-Ti metal matrix composite systems in the literature [13,14]. Inverse pole figure (IPF) maps from the EBSD analysis confirmed the presence of equiaxed grain structures in the coupons, in the NHT and both HT conditions (see **Figure 3 (g)-(i)**). The inoculant particles provided numerous heterogeneous nucleation sites for solidification, promoting grain refinement and formation of equiaxed grains. The particles (i.e., TiC and B₄C)

acted as grain boundary pinners that resisted grain growth after different HT conditions. The average grain sizes (measured in equivalent circle diameter) were consistent across all HT conditions of around $0.7\ \mu\text{m}$. The EDS elemental maps presented in **Figure 4** for NHT, HIP, and SR+HIP conditions confirm the presence of TiC and B₄C particles, and Al₃Fe and Ti₅Si₃ precipitates.

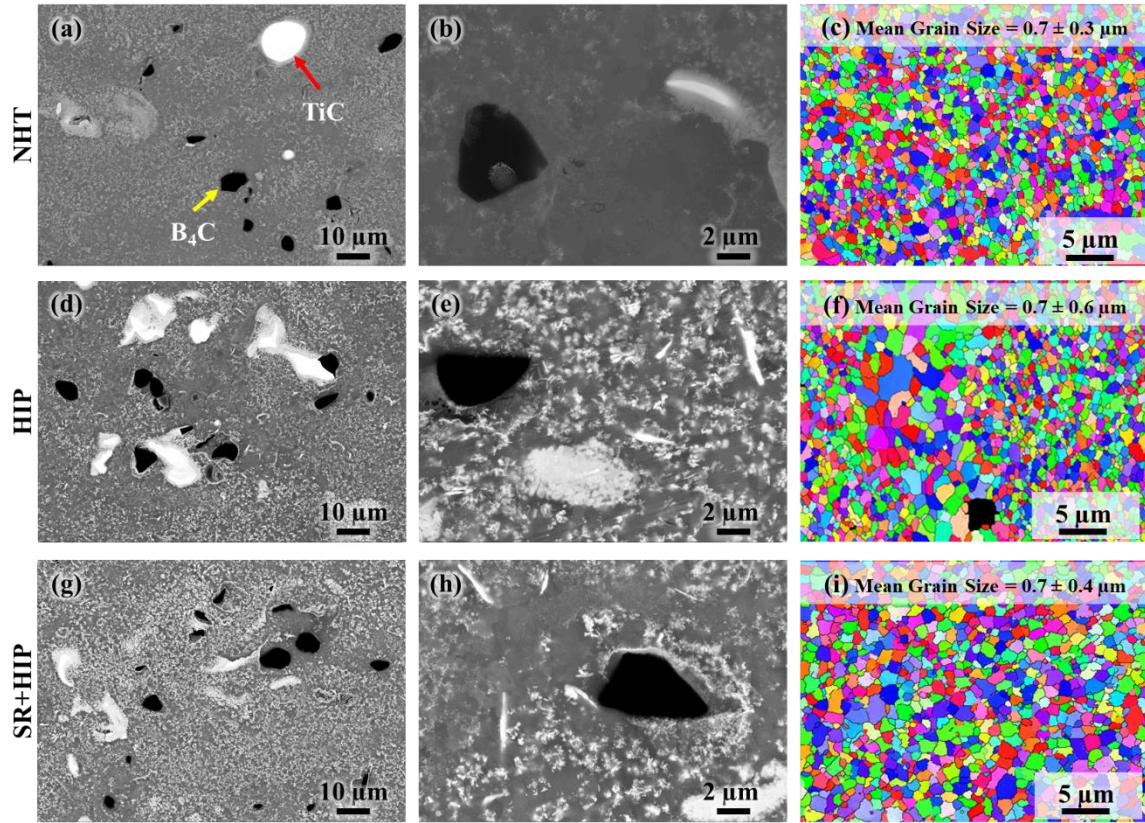


Figure 3. BSE micrographs and IPF maps of L-PBF A1000-RAM10 alloy in different HT conditions: (a)-(c) NHT, (d)-(f) HIP, and (g)-(i) SR+HIP.

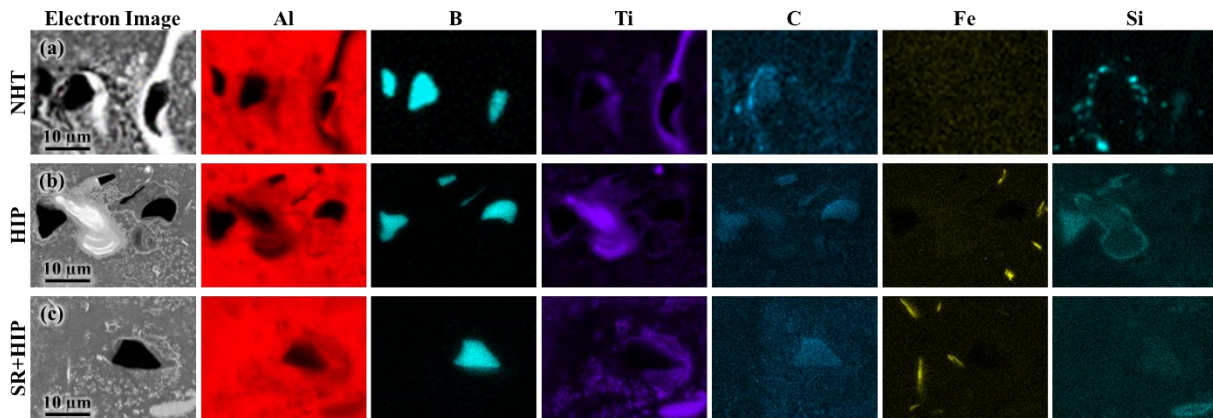


Figure 4. Results from EDS analysis, i.e., the elemental maps for L-PBF A1000-RAM10 alloy in: (a) NHT, (b) HIP, and (c) SR+HIP conditions.

The engineering stress-engineering strain curves and quasi-static tensile properties, including YS, UTS, and EL of L-PBF A1000-RAM10 specimens in NHT and two different HT conditions, are presented in **Figure 5(a)** and (b), respectively. These properties were compared with those of wrought (annealed) A1000 [15]. L-PBF specimens in all HT conditions showed significantly higher YS and UTS compared to the wrought counterpart. This enhancement can be attributed to two factors, i.e., grain boundary strengthening due to the finer grain structure, and the presence of TiC and B₄C particles, which contribute to strengthening by pinning grain boundaries and hindering dislocation motion. However, the YS and UTS of L-PBF A1000-RAM10 specimens remained comparable across NHT and both HT conditions. This can be attributed to stable grain structures and the presence of similar particles in all cases [7]. EL for L-PBF A1000-RAM10 specimens was comparable across all HT conditions but was significantly lower than that for the wrought counterpart (see **Figure 5(b)**). The tensile fracture surfaces of the specimens are shown in **Figure 6**, revealing similar fracture mechanisms across different HT conditions. The presence of TiC and B₄C particles promoted void nucleation, resulting in comparable EL for specimens from all HT conditions (see **Figure 6**).

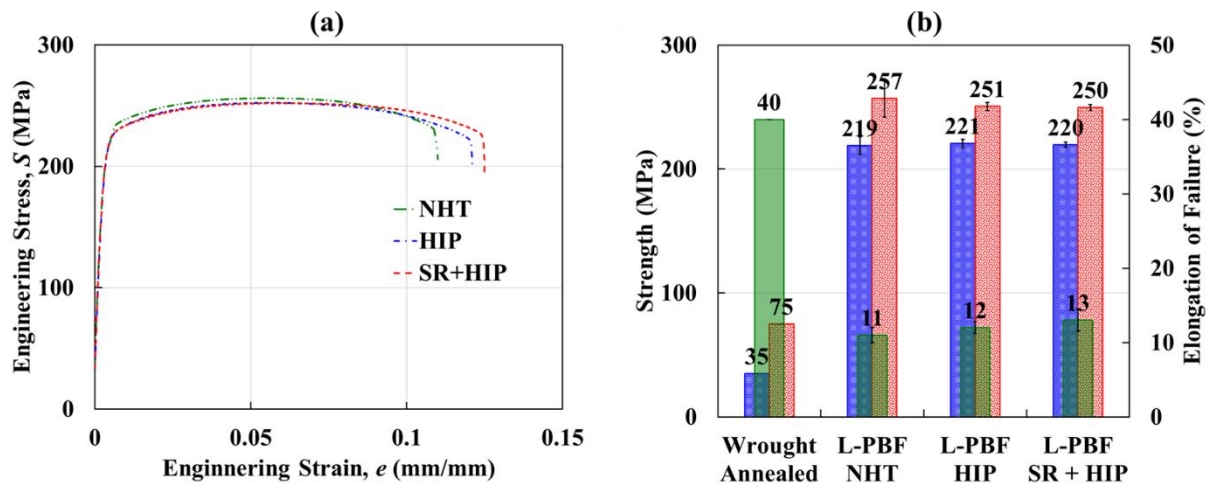


Figure 5. Tensile behavior of L-PBF A1000-RAM10 alloy in different HT conditions: (a) engineering stress-engineering strain curves and (b) comparative bar charts for tensile properties of L-PBF A1000-RAM10 obtained in this study as well as those of wrought (annealed) A1000 [15] from the literature.

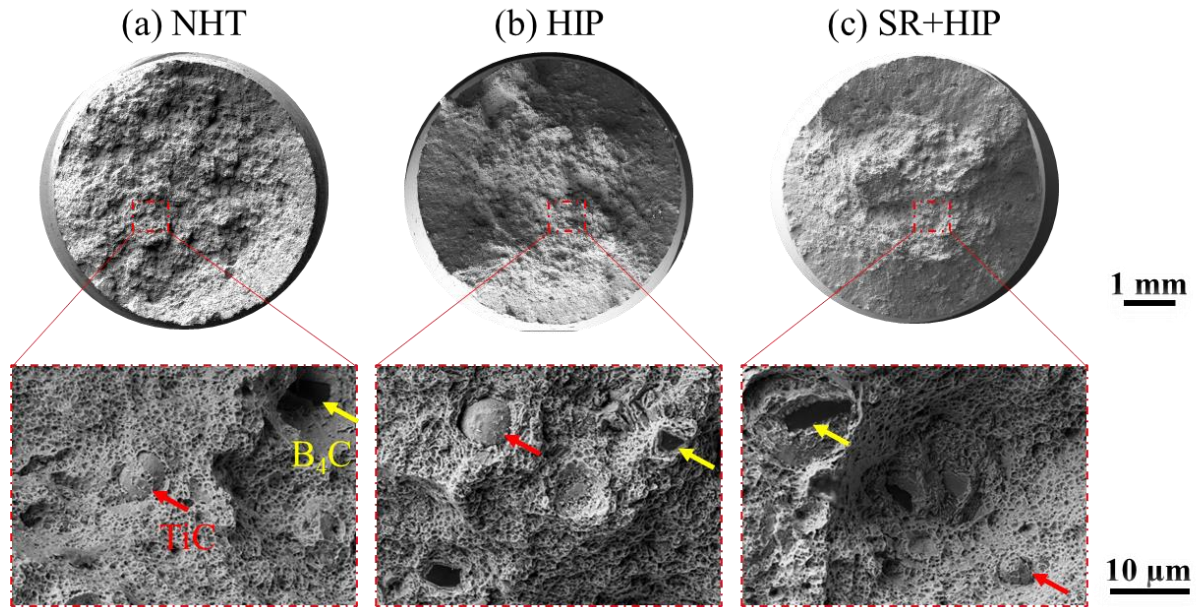


Figure 6. Tensile fracture surfaces of L-PBF A1000-RAM10 specimens in different HT conditions: (a) NHT, (b) HIP, and (c) SR+HIP. Red and yellow arrows indicate the TiC and B₄C particles, respectively.

Conclusion

This study investigated the effect of heat treatment (HT) on the defect content, microstructure, and room temperature tensile behavior of A1000-RAM10 alloy fabricated using laser powder bed fusion. The following conclusions were drawn:

- During solidification, the thermally stable B₄C and TiC particles acted as heterogeneous nucleation sites and grain boundary pinners, which resulted in a fine-grained and equiaxed microstructure. Moreover, the TiC and B₄C particles remained stable and present across all HT conditions, leading to a consistent grain structure.
- HTs incorporating hot isostatic pressing significantly reduced the overall population and size of volumetric defects.
- The yield strength, ultimate tensile strength, and elongation to failure were comparable among the different HT conditions due to consistent grain structure and presence of stable particles, such as TiC and B₄C.

Acknowledgment

This research is based upon the work partially supported by the National Aeronautics and Space Administration (NASA) contract 80MSFC19C0010 and the National Science Foundation (NSF) under grant No. 2319690. Reference herein to any specific commercial product, process, or service by trade name, trademark, manufacturer, or otherwise, does not constitute or imply its endorsement by NASA or the United States Government.

References

- [1] Vargel C. 1XXX Series. In: Vargel C, editor. *Corros. Alum. Second Edi*, Amsterdam: Elsevier; 2020, p. 447–51. <https://doi.org/10.1016/B978-0-08-099925-8.00030-2>.
- [2] Khan MF, Ghiaasiaan R, Gradl PR, Shao S, Shamsaei N. Additively Manufactured Scalmalloy via Laser Powder Bed Fusion (L-PBF): Temperature-Dependent Tensile and Fatigue Behaviors. *Fatigue Fract Eng Mater Struct* 2025;48:1496–513. <https://doi.org/10.1111/ffe.14549>.
- [3] Khan MF, Baig S, Ghiaasiaan SR, Gradl PR, Shao S, Shamsaei N. Effect of thermal post-processing on microstructure and tensile behavior of additively manufactured aluminum alloys (AlSi10Mg and Scalmalloy) via L-PBF: A comparative study. *Solid Free Fabr 2022 Proc 33rd Annu Int Solid Free Fabr Symp – An Addit Manuf Conf* 2022:341–53. <https://doi.org/10.26153/TSW/44158>.
- [4] Rahman MA, Saleh T, Jahan MP, McGarry C, Chaudhari A, Huang R, et al. Review of Intelligence for Additive and Subtractive Manufacturing: Current Status and Future Prospects. *Micromachines* 2023, Vol 14, Page 508 2023;14:508. <https://doi.org/10.3390/MI14030508>.
- [5] Khan MF, Nezhadfar PD, Gradl PR, Godfrey D, Diemann J, Shao S, et al. Investigate the height dependency of the micro-/defect-structure and mechanical properties of additively manufactured AlF357 aluminum alloy. *Int. Solid Free. Fabr. Symp.*, 2022, p. 302–13. <https://doi.org/10.26153/tsw/44148>.
- [6] Nuechterlein JS, Joseph Iten J. *Reactive additive manufacturing*. US10507638B2, 2021.
- [7] Khan MF, Ghiaasiaan R, Gradl PG, Firdosy S, Shao S, Shamsaei N. Effect of Heat Treatment on the Micro-/Defect-Structure and Tensile Behavior of Additively Manufactured A6061-RAM2 Aluminum Alloy. *2024 Int. SOLID Free. Fabr. Symp.*, 2024, p. 685–98. <https://doi.org/10.26153/tsw/58106>.
- [8] ASTM International. *ASTM E1409-13 Standard Test Method for Determination of Oxygen and Nitrogen in Titanium and Titanium Alloys by Inert Gas Fusion*. West Conshohocken, PA 19428-2959 USA 2021. <https://doi.org/10.1520/E1409-13R21>.
- [9] ASTM International. *ASTM E1019-18 Standard Test Methods for Determination of Carbon, Sulfur, Nitrogen, and Oxygen in Steel, Iron, Nickel, and Cobalt Alloys by Various Combustion and Inert Gas Fusion Techniques*. West Conshohocken, PA 19428-2959 USA 2018. <https://doi.org/10.1520/E1019-18>.

- [10] SAE Aerospace. AMS2770: Heat Treatment of Wrought Aluminum Alloy Parts. *Aerosp Mater Specif* AMS2770 2011;Rev. J.
- [11] ASTM E3-11. Guide for Preparation of Metallographic Specimens. *ASTM Stand* 2017;03.01:1–12. <https://doi.org/10.1520/E0003-11R17>.
- [12] ASTM E8. Test Methods for Tension Testing of Metallic Materials. *ASTM Stand* 2024:1–27. https://doi.org/10.1520/E0008_E0008M-24.
- [13] Griger A, Stefániay V, Kovács-Csetényi E, Turmezey T. Formation and Transformation of Binary Intermetallic Phases in High Purity Al-Fe Alloys. *Key Eng Mater* 1991;44–45:17–30. <https://doi.org/10.4028/www.scientific.net/KEM.44-45.17>.
- [14] Rajan TPD, Pillai RM, Pai BC. Reinforcement coatings and interfaces in aluminium metal matrix composites. *J Mater Sci* 1998;33:3491–503. <https://doi.org/10.1023/A:1004674822751>.
- [15] ASM International Handbook Committee. *ASM Handbook Vol. 2: Properties and Selection: Nonferrous Alloys and Special-Purpose Materials*. 2001.